

# PARAMETER-UNIFORM SUPERCONVERGENCE OF MULTISCALE COMPUTATION FOR SINGULAR PERTURBATION EXHIBITING TWIN BOUNDARY LAYERS\*

Shan Jiang<sup>1,†</sup>, Xiao Ding<sup>1</sup> and Meiling Sun<sup>2</sup>

**Abstract** We propose a multiscale finite element scheme on a graded mesh for solving a singularly perturbed convection-diffusion problem efficiently. Twin boundary layers phenomena are shown in the one-dimensional model, and an adaptively graded mesh is applied to probe the twin boundary jumps. We evoke an updated multiscale strategy through the multiscale basis functions in a linear Lagrange style. Detailed mapping behaviors are investigated on fine as well as on coarse scales, thus incorporating information at the micro-scale into the macroscopic data. High-order stability theorems in an energy norm of multiscale errors are addressed. Our approach can achieve a parameter-uniform superconvergence with limited computational costs on the coarse graded mesh. Numerical results support the high-order convergence theorem and validate the advantages over other prevalent methods in the literature, especially for the singular perturbation with very small parameters. The proposed method is twin boundary layers resolving as well as parameter uniform superconvergent.

**Keywords** Singularly perturbed problem, adaptive mesh, multiscale finite element method, superconvergence, mapping matrix.

**MSC(2010)** 65L11, 65L50, 65L60.

## 1. Introduction

Singular perturbation problems are encountered in many fields like fluid dynamics, quantum mechanics, turbulent waves, biochemical reactors, magneto-hydrodynamic flows, and optimal control. The differential equations have small perturbation parameters, which always appear as the coefficient in the highest-order term. Due to the existence of small parameters, the problem would exhibit a so-called boundary layer phenomenon, which means although the solution is bounded, it involves

---

<sup>†</sup>The corresponding author.

<sup>1</sup>School of Science, Nantong University, Nantong 226019, China

<sup>2</sup>Department of Mathematics, Nantong Vocational University, Nantong 226007, China

\*The authors were supported by National Natural Science Foundation of China (11771224, 12171258) and by Nantong injunctive projects for basic scientific research (JC2021123).

Email: [jiangshan@ntu.edu.cn](mailto:jiangshan@ntu.edu.cn)(S. Jiang), [1053471033@qq.com](mailto:1053471033@qq.com)(X. Ding), [sunmeiling81@163.com](mailto:sunmeiling81@163.com)(M. L. Sun)

extremely large derivatives in certain thin layers near the domain boundary. It is important to study these problems to understand the interaction between convection and diffusion.

Robust approaches have been analyzed the behavior of singular perturbations, such as the finite element method [2, 4, 10, 22, 25, 33], finite difference method [5, 15, 27, 28], B-spline collocation method [20, 21, 26], reproducing kernel method [13], asymptotic expansion method [32], local discontinuous Galerkin method [6–8], and the multiscale method [9, 16, 17]. Discretization was used on a class of layer-adapted meshes [1, 24, 29, 30] and on hybrid meshes [25] to address the proper status of the boundary layers. Combined with an appropriate method, they are conducive to solving the simulation dilemma in the singular perturbation problems. For instance, a convection-reaction-diffusion equation is studied by the standard bilinear finite elements on Duran-Lombardi and Duran-Shishkin meshes in Brdar et al. [3], and the first-order error estimate in an energy norm was proved. Sharma et al. [31] have reviewed the literature from 1970 and 2011 on numerical and asymptotic analysis for problems with turning points and interior layers. As for the twin boundary layers, [13, 19, 20, 27] provide many enlightening insights. Such as Natesan et al. [27] applied a classical upwind difference scheme on a piecewise Shishkin mesh to resolve the solution decomposition. However, we know that there is still much room for improvement in terms of accuracy and efficiency. Kadalbajoo and Gupta [20] presented a cubic B-spline collocation on the Shishkin mesh. In comparison, our work shows that just a linear Lagrange style basis function would outperform it in terms of accuracy.

In recent works, Kumar [23] offered a quintic B-spline collocation method with a parameter-uniform result, which is a nice contrast to our study. Gupta et al. [15] proposed another parameter-uniform, high order, finite difference scheme for a time-dependent parabolic problem with two small parameters. Kaushik et al. [22] generated a graded mesh from some implicit functions and used a high-order FEM to achieve the high-order convergence. Brdar et al. [1] solved a convection-diffusion equation using FEM and SDFEM with bilinear elements on a graded mesh to attain superconvergence. Cheng et al. [8] verified the convergent order of  $(N^{-1} \max |\psi'|)^{k+1/2}$  energy norm on the Bakhvalov-Shishkin mesh and Bakhvalov-type mesh. Cheng, Jiang, and Stynes [7] derived a supercloseness result for a singularly perturbed convection-diffusion problem using the LDG method on three layer-adapted meshes and the local Gauss-Radau projection. Furthermore, they presented a delicate argument to establish a superconvergence of  $\mathcal{O}(N^{-(k+1)})$  in the energy norm error. These works suggest that highly efficient multiscale strategies could be devised on an updated graded mesh to achieve superconvergence. Govindarao and Mohapatra [14] reported a numerical scheme to solve a parabolic-elliptic mixed type problem. Both boundary and interior layers appeared in the spatial variable in their solution. The implicit Euler scheme and the Crank-Nicolson scheme on a uniform mesh were used for time-stepping, while the central difference scheme and a hybrid scheme on Shishkin-type meshes were used for spatial discretization. We have addressed multiscale computation for singularly perturbed 1D and 2D problems in our previous publications [16–18]. Elmahdi and Huang [12] presented a linearized alternating direction implicit scheme for 2D time-space fractional nonlinear diffusion-wave equation and discussed its unconditional stability.

In this paper, a singularly perturbed convection-diffusion problem is considered

$$\begin{cases} Lu := -\varepsilon u''(x) + b(x)u'(x) + c(x)u(x) = f(x), & \text{in } \Omega = (0, 1), \\ u(0) = u_0, \quad u(1) = u_1, \end{cases} \quad (1.1)$$

where  $\varepsilon$  is a small positive parameter,  $b(x)$  and  $c(x)$  are coefficients, and  $f(x)$  is the source term. These are all sufficiently regular functions with properties

$$|b(x)| \geq 2\beta > 0, \quad c(x) \geq 0, \quad c(x) - \frac{1}{2}b'(x) \geq c_0 > 0, \quad \forall x \in \bar{\Omega} = [0, 1].$$

Then  $b(0) < 0$  and  $b(1) > 0$ , twin boundary layers at  $x = 0, 1$  are expected as it is known from the non-turning point problem.

The solution  $u(x)$  and its  $k$ -th order of derivative satisfies the following relation

$$|u^{(k)}(x)| \leq C(1 + \varepsilon^{-k} \cdot e(x, \beta, \varepsilon)), \quad k = 0, 1, \dots, q \in \mathbb{N}, \quad (1.2)$$

where  $e(x, \beta, \varepsilon) = \exp^{-\frac{\beta x}{\varepsilon}} + \exp^{-\frac{\beta(1-x)}{\varepsilon}}$ . For a small parameter  $0 < \varepsilon \ll 1$ ,  $u(x)$  may show boundary layers phenomena at the twin boundaries near both the left and right endpoint  $x = 0$  and/or  $x = 1$ .

The characteristic equation for (1.1) is  $-\varepsilon\lambda^2(x) + b(x)\lambda(x) + c(x) = 0$ , and its real roots  $\lambda_1(x) < 0, \lambda_2(x) > 0$ . Denote that

$$\begin{aligned} \mu_1 &= -\max_{x \in [0, 1]} \lambda_1(x), \\ \mu_2 &= \min_{x \in [0, 1]} \lambda_2(x). \end{aligned}$$

Then

$$\mu_1 = \min_{x \in [0, 1]} \frac{-b(x) + \sqrt{b^2(x) + 4\varepsilon c(x)}}{2\varepsilon}, \quad (1.3)$$

$$\mu_2 = \min_{x \in [0, 1]} \frac{b(x) + \sqrt{b^2(x) + 4\varepsilon c(x)}}{2\varepsilon}. \quad (1.4)$$

The values  $\mu_1$  and  $\mu_2$  determine the decay of boundary layers. Except the normal scale  $O(1)$ , they are expressed as the characteristic scale  $O(\frac{1}{\varepsilon})$ .

In the singular perturbation, the solution possesses a multiscale nature, presenting rapid variations in narrow regions close to both the left and right boundaries. The multiscale nature of  $u(x)$  could be explored in the scale decompositions. That is, an inner smooth component  $S(x)$  and two singular components  $E_1(x)$  and  $E_2(x)$  read

$$u(x) = S(x) + E_1(x) + E_2(x) = S(x) + E(x). \quad (1.5)$$

**Lemma 1.1.** [6] *If  $b(x), c(x), f(x) \in C^{k+2}(\bar{\Omega})$ , where  $k \in \mathbb{N}^+$  and let  $p \in (0, 1)$  be arbitrary. Then the derivatives of decomposition (1.5) are bounded,*

$$\begin{aligned} |S^{(k)}(x)| &\leq C, \\ |E_1^{(k)}(x)| &\leq C\mu_1^k \exp^{-p\mu_1 x}, \\ |E_2^{(k)}(x)| &\leq C\mu_2^k \exp^{-p\mu_2(1-x)}. \end{aligned}$$

We are inclined to pursue the optimal approximation of the solution and its derivatives, especially in the singular component  $E(x)$ .

As for a bilinear form

$$a(u, v) = \varepsilon(u', v') + (bu' + cu, v), \quad (1.6)$$

and an inner product

$$(f, v) = \int_{\Omega} f v dx, \quad (1.7)$$

thus a variational formulation of (1.1) is to find a trial function  $u \in H^1(\Omega)$  such that

$$a(u, v) = (f, v), \quad \text{for } \forall v \in H_0^1(\Omega), \quad (1.8)$$

where  $v$  is a test function.

As usual, standard Sobolev spaces  $W^{m,p}(\Omega)$ ,  $L^p(\Omega) = W^{0,p}(\Omega)$ ,  $H^m(\Omega) = W^{m,2}(\Omega)$ ,  $H_0^m(\Omega)$  are used, and  $(\cdot, \cdot)$  is used for a  $L^2(\Omega)$  inner product. Related norm and seminorm are  $\|\cdot\|_{m,p,\Omega}$  and  $|\cdot|_{m,p,\Omega}$ , respectively defined on  $W^{m,p}(\Omega)$ . A simplification is  $\|\cdot\|_m = \|\cdot\|_{m,2,\Omega}$  and  $|\cdot|_m = |\cdot|_{m,2,\Omega}$ , for the case  $p = 2$ . We introduce an  $\varepsilon$ -weighted energy norm as

$$\|\cdot\|_{\varepsilon}^2 = \|\cdot\|_0^2 + \varepsilon\|\cdot\|_1^2. \quad (1.9)$$

It is used to testify errors between the exact solution and its numerical solution. Throughout the paper,  $C$  indicates a generic independent constant.

This paper is characterized by the features: 1. The key feature of our work is the accuracy and efficiency of the multiscale finite element scheme for the singular perturbation problem achieved using the multiscale basis functions in the local problems for investigating the micro-scale boundary regions. The delicate mapping behavior between the fine scales and the coarse ones is presented and a reduced algebraic system is solved on the coarse-scale level, yielding solutions with good precision and adequate efficiency.

2. A modified recursion of the graded mesh is updated to implement spatial discretization in several intervals for the one-dimensional convection-diffusion model exhibiting twin boundary layers. It is closely related to a mesh-generating function and its mesh-characterizing counterpart, for adaptively capturing the twin boundary layers. Note that the available grid nodes are ready to be utilized in the multiscale approach on its coarse-scale level, and only the linear multiscale basis functions are employed, thus decreasing the computation needed.

3. A stable error estimate with high-order convergence in the energy norm is determined. Parameter-uniform superconvergence results are illustrated theoretically as well as experimentally, particularly for small perturbation parameters. Numerical experiments show that this approach is robust and economical as compared to other methods. Furthermore, this approach can also be potentially applied to high-dimensional problems.

The paper proceeds as follows. In Section 2, several layer-adapted meshes are reviewed, and a modified graded mesh with the adaption is provided for the twin boundary layers. In Section 3, we devise a multiscale finite element scheme, in which the multiscale basis functions bridge the mapping details between the fine- and the coarse-scales. It can be seen that our multiscale strategy is superior to

the traditional method in terms of its efficiency as well its applicability. Multiscale error analyses on the parameter-uniform superconvergence are exhibited in Section 4. In Section 5, numerical results are presented. Finally, our concluding remarks are provided in Section 6.

## 2. Mesh discretization and adaption

### 2.1. Several discretizations

The various mesh partitioning schemes for the finite-dimensional discretization of the domain  $\Omega$  are described in this section. Suppose that the model (1.1) has a large parameter  $\varepsilon$ . In this case, there are no boundary layers and traditional methods work well. It is known that a uniform mesh is sufficient to satisfy the condition  $h < \varepsilon$  for a large parameter  $\varepsilon$  (whose mesh size  $h = 1/N$  is a constant, where  $N$  is the number of mesh partition). However, as for a small parameter  $\varepsilon$ , the model is likely to produce boundary layers with widths  $O(\tau) = O(\varepsilon \log N)$ . In this case, it is hard to satisfy the condition  $h < \varepsilon$  even with a very huge partition number  $N$ , which would lead to an unreliable result.

For the case where  $\varepsilon$  is small, the domain  $\Omega$  can be divided into smooth and singular components according to a transition point  $\tau = \min\{\frac{1}{2}, \frac{\varepsilon \log N}{\beta}\}$ . Based on an *a priori* estimate we can try to estimate the approximate locations of boundary layers, and employ several non-uniform meshes. Here the total partition number  $N$  is predetermined and fixed. Hence, half of it is refined to depict the singular components, while the other half may be coarsened to depict the smooth component. This  $h$ -adapted strategy may be described as follows.

First a Shishkin mesh is outlined. Suppose that the boundary layer appears near the right side  $x = 1$ . Then  $\bar{\Omega} = [0, 1]$  is divided into the subdomains  $[0, 1 - \tau]$  and  $[1 - \tau, 1]$ , and both subdomains are partitioned in  $N/2$  elements. The grid nodes are

$$\text{Shishkin: } x_i = \begin{cases} \frac{2(1-\tau)}{N} \cdot i, & i = 0, \dots, \frac{N}{2}, \\ 1 - \tau + \frac{2\tau}{N} \cdot (i - \frac{N}{2}), & i = \frac{N}{2} + 1, \dots, N. \end{cases} \quad (2.1)$$

Next, a Bakhvalov mesh in [29] is reviewed. Its distribution is derived from  $\exp^{-\frac{\beta(1-x_i)}{\varepsilon}} = Ai + B$  and  $x_{\frac{N}{2}} = 1 - \tau$ ,  $x_N = 1$ . In this way, the grid nodes are

$$\text{Bakhvalov: } x_i = \begin{cases} (1 - \frac{\varepsilon}{\beta} \log N) \cdot \frac{2i}{N}, & i = 0, \dots, \frac{N}{2}, \\ 1 + \frac{\varepsilon}{\beta} \log[1 - 2(1 - \frac{1}{N})(1 - \frac{i}{N})], & i = \frac{N}{2} + 1, \dots, N. \end{cases} \quad (2.2)$$

Note that in this subsection, the partition number  $N$  is pre-determined and is always an even number  $2^l$  ( $l \in \mathbb{N}^+$ ) for the double refinement.

### 2.2. Graded mesh adaption

Durán and Lombardi [11], Roos et al. [30] have proposed more flexible improvements, that include a highly anisotropic, nonuniform, graded mesh based on a recursive iteration, where the grid nodes are determined by the initial constants,

$0 < h < 1$  and  $\sigma > 0$ , for mesh generation. In the expressions below, we have taken  $h = 0.5$  and  $\sigma = 1$ . One should keep in mind that in this case,  $N$  is no longer a fixed number and that it satisfies  $x_{N-1} < 1$  and  $(1 + \sigma h)x_{N-1} \geq 1$ . A large number of grid nodes would be concentrated on the left side  $x = 0$  through

$$x_i = \begin{cases} 0, & i = 0, \\ \sigma h \varepsilon, & i = 1, \\ (1 + \sigma h)x_{i-1}, & 2 \leq i \leq N - 1, \\ 1, & i = N. \end{cases} \tag{2.3}$$

On the other hand, if the boundary layer appears near the right side  $x = 1$ , the generated arrays could be flipped from the left to the right using the command *ones-fliplr* in our MATLAB code. As a result, these non-uniform nodes will be concentrated on the right side contrarily. Furthermore, the partition number  $N$  could be any random positive integers generated by the recursive algorithm. The numbers output is given in Section 5.

For a more general case, let us suppose that the singular perturbation dominates on both sides,  $x = 0$  and  $x = 1$ . We can provide a graded mesh iteration for twin boundary layers as given below:

$$\text{Graded: } x_i = \begin{cases} 0, & i = 0, \\ \sigma h \varepsilon, & i = 1, \\ (1 + \sigma h)x_{i-1}, & 2 \leq i \leq N_0 - 1, \\ 0.5, & i = N_0, \\ 1 - (1 + \sigma h)(1 - x_{i+1}), & N_0 + 1 \leq i \leq N - 2, \\ 1 - \sigma h \varepsilon, & i = N - 1, \\ 1, & i = N, \end{cases} \tag{2.4}$$

here  $N_0$  is the original number  $N$  in (2.3). It will result in a quasi-symmetric mesh discretization. The graded mesh adaption can be efficiently applied to the problem exhibiting twin boundary layers. This is a fitting mesh for approaching the transition points.

Let us set  $\alpha = k + 1$  in the paper, where  $k \in \mathbb{N}^+$  is the degree of the polynomial, or the order of derivative. The mesh-generating functions are used to probe the locations of twin boundary layers. The transition point  $\tau$  can be determined later for the decomposition of intervals (1.5). Set

$$x_0 = 0, \quad x_{\frac{N}{4}} = \tau, \quad x_{\frac{3N}{4}} = 1 - \tau, \quad x_N = 1,$$

thus resulting in the formation of a left singular component  $[0, \tau]$ , a right singular component  $[1 - \tau, 1]$ , and an inner smooth sub-domain  $[\tau, 1 - \tau]$ . If we define  $t_i$  as

$$t_i = \frac{i}{N}, \quad i = 0, 1, \dots, N, \tag{2.5}$$

then the graded nodes can be constructed as shown:

$$x_i = \alpha\varepsilon g\left(\frac{i}{N}\right) = \alpha\varepsilon g(t_i). \quad (2.6)$$

The mesh-generating function  $g(t_i)$  is provided such that

$$g(0) = 0, \quad g\left(\frac{1}{4}\right) = \log N, \quad g\left(\frac{3}{4}\right) = \frac{1 - \alpha\varepsilon \log N}{\alpha\varepsilon}, \quad g(1) = \frac{1}{\alpha\varepsilon}.$$

Hence,  $\tau = \min\{\frac{1}{2}, \alpha\varepsilon g(\frac{1}{4}), \alpha\varepsilon g(\frac{3}{4})\}$ , whose approximate location is dependent on  $\alpha$ ,  $\varepsilon$  and  $N$ . The mesh-generating function  $g$  is thus closely related to the mesh-characterizing function  $\omega$  as shown below:

$$g = -\log \omega \Leftrightarrow \omega = \exp^{-g} = C_1 \exp^{-\frac{x_i}{\alpha\varepsilon}} + C_2 \exp^{-\frac{(1-x_i)}{\alpha\varepsilon}}. \quad (2.7)$$

From the view of eigenvalue scales of  $\mu_1$  in (1.3) and  $\mu_2$  in (1.4), the function  $\omega$  could also be represented as

$$\omega = C_1 \exp^{-\frac{p\mu_1 x_i}{\alpha}} + C_2 \exp^{-\frac{p\mu_2 (1-x_i)}{\alpha}}, \quad p \in (0, 1). \quad (2.8)$$

We can see that the graded mesh is not of a pre-determined type, and it relies on the recursive iteration in Eq. (2.4), whose initial parameter  $h$ ,  $\sigma$ , and the perturbation parameter  $\varepsilon$  can be chosen. Once the graded nodes  $x_i$  are available, a varying mesh size  $h_i = x_i - x_{i-1}$  is used in the  $i$ -th element  $K$ . It can be confirmed that the mesh size is either monotonically increasing or decreasing, and that this mesh is prepared for the multiscale finite element computation on the coarse level as shown in the sections that follow. The advantage of the graded mesh is that it may adaptively adjust to the local behavior of the original problem, and it is shown to be optimal for capturing the behavior of twin boundary layers accurately and economically in our multiscale simulation.

### 3. Multiscale strategy

#### 3.1. Finite element scheme

Let us consider a finite element space

$$V^h = \text{span}\{\psi_i\}_{i=0}^{N_{b1}} \subset H^1(\Omega), \quad (3.1)$$

where the finite element basis functions  $\psi_i$  form a basis of  $V^h$ , and  $N_{b1}$  is the global number in the FE scheme. Let us denote an element by  $K$  and the corresponding mesh partition by  $\mathcal{K}^h$  (for any  $K \in \mathcal{K}^h$ ). We can find the Galerkin FEM solution  $u_g \in V^h$  using the finite element method such that

$$a(u_g, v) = (f, v), \quad \forall v \in V^h. \quad (3.2)$$

However, for the case of a small parameter  $\varepsilon$  in (1.1), the boundary layers phenomena can be quite troublesome, as the solution, and especially its derivative would be extremely large. We aim to achieve very accurate and convergent solutions that are independent of the value of the perturbation parameter, while simultaneously minimizing the computations needed. From this point of view, we would like to present a novel strategy for the multiscale finite element method on an adaptively graded mesh, which offers sufficient accuracy with moderate costs, and grants a parameter-uniform superconvergence for the singular perturbation.

### 3.2. Multiscale finite element scheme

In contrast to Galerkin FEM, the multiscale space can be enriched with the multiscale basis functions  $\phi_i$  as shown

$$U^h = \text{span}\{\phi_i, \quad \forall K \in \mathcal{K}^h\}. \tag{3.3}$$

These multiscale bases  $\phi_i$  have strengths to reflect the microscopic information of the macroscopic problem (1.1), and they may capture the local perturbation in boundary layers. We will further see that the space  $U^h$  represents the unresolvable scales. This is achieved by evolving the local problems in the finite element scheme.

The multiscale basis functions are investigated in each coarse element  $K$ , as shown below:

$$\begin{cases} L\phi_i := -\varepsilon\phi_i''(x) + b(x)\phi_i'(x) + c(x)\phi_i(x) = 0, & \text{in } K, \\ \phi_i = \psi_i, & \text{on } \partial K. \end{cases} \tag{3.4}$$

The boundary condition for  $\phi_i$  is the known finite element basis function  $\psi_i$ . We can see that the local problem (3.4) and the original problem (1.1) have an identical differential operator  $L$ . The core difference is that (1.1) is solved directly using FEM, while (3.4) is solved for the multiscale basis functions indirectly in the coarse elements. Consequently, the microscopic information of boundary layers is captured through the multiscale bases  $\phi_i$  on the coarse-scale level. We should point out that this is quite different from the classical FEM, which is entirely computed on the fine-scale level and would have more computational costs. Hence, the multiscale strategy is used to find the  $u_h \in U^h$  such that

$$a(u_h, v) = (f, v), \quad \forall v \in U^h, \tag{3.5}$$

where  $u_h$  is the MsFEM solution.

**Lemma 3.1.** *Assume that there are twin boundary layers on both sides, and that the mesh size  $h_i = x_i - x_{i-1}$ , recall  $\mu_1$  in (1.3),  $\mu_2$  in (1.4), and  $p \in (0, 1)$ ,  $\alpha = k + 1$ . Let us denote*

$$\begin{aligned} \mathcal{G}_i^L &= \min\{h_i\mu_1, 1\} \exp^{-\frac{p\mu_1 x_i}{\alpha}}, \quad i = 0, 1, \dots, \frac{N}{4}, \\ \mathcal{G}_i^R &= \min\{h_i\mu_2, 1\} \exp^{-\frac{p\mu_2(1-x_i)}{\alpha}}, \quad i = \frac{3N}{4} + 1, \dots, N. \end{aligned}$$

Then we have

$$\max_{0 \leq i \leq N/4} \mathcal{G}_i^L \leq CN^{-1} \max |\omega'|^\alpha, \tag{3.6}$$

$$\max_{3N/4+1 \leq i \leq N} \mathcal{G}_i^R \leq CN^{-1} \max |\omega'|^\alpha. \tag{3.7}$$

**Proof.** Please refer to Cheng [6] for similar details. □

Even though the width  $\tau$  of the left boundary layer in  $\Omega_1 = [0, \tau]$  and the right boundary layer in  $\Omega_3 = [1 - \tau, 1]$  is very small, it would still occupy a quarter of



**Figure 1.** For  $N = 4$  and  $M = 2$ , solid points to represent  $N + 1 = 5$  coarse grid nodes, together with hollow points to represent  $N * M + 1 = 9$  fine grid nodes in all.

partition number  $N/4$ , respectively. While the width of the smooth component  $\Omega_2 = [\tau, 1 - \tau]$  is much more larger, it occupies the other half of partition number  $N/2$  for discretization.

As described above, the graded nodes derived from the recursive formula (2.4) are not like the piece uniform Bakhvalov-Shishkin and Duran-Shishkin nodes whose partition number  $N$  is pre-determined. However, the graded nodes can detect the location of the transition point precisely and can concentrate on the boundary layers. When the mesh parameter  $h$  decreases, the partition number  $N$  increases. These features will enable the graded mesh to approach twin boundary layers effectively and significantly reduce boundary layer errors. The simulation behavior and the multiscale finite element strategy are presented in Section 4 and 5.

For solving the local problem (3.4), sub-partitions are necessary for each coarse element  $K$ . In this paper, we have applied finite element schemes for solving multi-scale basis functions. The finite element scheme may use linear or high-order basis functions, whose computational costs could increase accordingly. For simplicity, let us take the option of linear Lagrange basis function as explained below. First, a coarse-scale partition number  $N$  is determined for the whole domain  $\bar{\Omega}$ . Then, a fine-scale partition number  $M$  is determined for each coarse element  $\bar{K}_i = [x_{i-1}, x_i]$ . Then each coarse element has  $M + 1$  fine nodes as given by

$$x_{i-1} = x_{i-1,0} < x_{i-1,1} < \cdots < x_{i-1,M} = x_i,$$

where

$$x_{i-1,j+1} - x_{i-1,j} = \frac{x_i - x_{i-1}}{M}, \quad j = 0, \cdots, M - 1.$$

The multiscale basis function  $\phi_i$  is represented by

$$\phi_i = \sum_{j=0}^M r_{ij} \psi_j, \quad i = 0, \cdots, N, \quad (3.8)$$

where  $\psi_j$  is the known finite element basis function on the boundary in (3.4), and  $r_{ij}$  is the coefficient to be determined.

For instance, let us take a coarse partition number  $N = 4$  and a fine partition number  $M = 2$  in each coarse element, then global nodes are to be identified, see Fig 1. In (3.8) a block matrix for multiscale basis functions  $\phi_i$  is formed as shown

below:

$$\begin{bmatrix} \phi_0 \\ \phi_1 \\ \phi_2 \\ \phi_3 \\ \phi_4 \end{bmatrix} = \begin{bmatrix} r_{00} & r_{01} & r_{02} & & & & & & & \\ r_{10} & r_{11} & r_{12} & r_{13} & r_{14} & & & & & \\ & & r_{22} & r_{23} & r_{24} & r_{25} & r_{26} & & & \\ & & & & r_{34} & r_{35} & r_{36} & r_{37} & r_{38} & \\ & & & & & & & & r_{46} & r_{47} & r_{48} \end{bmatrix} \begin{bmatrix} \psi_0 \\ \psi_1 \\ \psi_2 \\ \psi_3 \\ \psi_4 \\ \psi_5 \\ \psi_6 \\ \psi_7 \\ \psi_8 \end{bmatrix}. \tag{3.9}$$

Thus, the corresponding coefficients  $r_{ij}$  for the multiscale basis functions are stored as block matrix entries into a mapping matrix  $R = (r_{ij})$ .

Then the elementary stiffness matrix and the elementary load vector are assembled to the global stiffness matrix and the global load vector, respectively. Note that it is only processed on the coarse-scale level. In the weak formulation (3.5), whose global stiffness matrix on the coarse-scale level  $A^c = (a_{ij}^c)$ . From (1.6) it reads

$$\begin{aligned} a_{ij}^c &= a(\phi_i, \phi_j) \\ &= \sum_{m=0}^M \sum_{n=0}^M r_{im} r_{jn} \int_K [\varepsilon(\psi_m)'(\psi_n)' + b(\psi_m)'\psi_n + c\psi_m\psi_n] dx. \end{aligned} \tag{3.10}$$

Similarly, the global load vector on the coarse-scale level  $b^c = (b_i^c)$ . From (1.7) it reads

$$b_i^c = (f, \phi_i) = \sum_{m=0}^M r_{im} \int_K f \psi_m dx. \tag{3.11}$$

Let  $A^f = (a_{st}^f)$  as the global stiffness matrix on the fine-scale level, to facilitate a better comparison. So, its relationship with the mapping matrix  $R$  may be expressed as shown below:

$$A^c = R A^f R^T, \tag{3.12}$$

where  $R^T$  is the transpose of  $R$ . Similarly, let  $b^f = (b_s^f)$  as the global load vector on the fine-scale level. We then have

$$b^c = R b^f. \tag{3.13}$$

For example, in the multiscale strategy let us take the first coarse element  $\bar{K}_1 = [x_0, x_1]$  in Fig 1. From (3.8) it reads

$$\begin{bmatrix} \phi_0 \\ \phi_1 \end{bmatrix} = \begin{bmatrix} r_{00} & r_{01} & r_{02} \\ r_{10} & r_{11} & r_{12} \end{bmatrix} \begin{bmatrix} \psi_0 \\ \psi_1 \\ \psi_2 \end{bmatrix} = R_{\text{loc}} \begin{bmatrix} \psi_0 \\ \psi_1 \\ \psi_2 \end{bmatrix}, \tag{3.14}$$

where  $R_{\text{loc}}$  is a local mapping matrix of  $R$ . Consequently, the elementary stiffness matrix in the multiscale scheme may be expressed as

$$\begin{aligned} & \begin{bmatrix} a(\phi_0, \phi_0) & a(\phi_0, \phi_1) \\ a(\phi_1, \phi_0) & a(\phi_1, \phi_1) \end{bmatrix} \\ &= \begin{bmatrix} r_{00} & r_{01} & r_{02} \\ r_{10} & r_{11} & r_{12} \end{bmatrix} \begin{bmatrix} a^f(\phi_0, \phi_0) & a^f(\phi_0, \phi_1) \\ a^f(\phi_1, \phi_0) & a^f(\phi_1, \phi_1) & a^f(\phi_1, \phi_2) \\ & a^f(\phi_2, \phi_1) & a^f(\phi_2, \phi_2) \end{bmatrix} \begin{bmatrix} r_{00} & r_{10} \\ r_{01} & r_{11} \\ r_{02} & r_{12} \end{bmatrix} \\ &= R_{\text{loc}} \begin{bmatrix} a^f(\phi_0, \phi_0) & a^f(\phi_0, \phi_1) \\ a^f(\phi_1, \phi_0) & a^f(\phi_1, \phi_1) & a^f(\phi_1, \phi_2) \\ & a^f(\phi_2, \phi_1) & a^f(\phi_2, \phi_2) \end{bmatrix} R_{\text{loc}}^T. \end{aligned}$$

Similarly, the elementary load vector in the multiscale scheme is given by

$$\begin{aligned} \begin{bmatrix} b_0^c \\ b_1^c \end{bmatrix} &= \begin{bmatrix} r_{00} & r_{01} & r_{02} \\ r_{10} & r_{11} & r_{12} \end{bmatrix} \begin{bmatrix} \int_K f \psi_0 dx \\ \int_K f \psi_1 dx \\ \int_K f \psi_2 dx \end{bmatrix} \\ &= R_{\text{loc}} \begin{bmatrix} \int_K f \psi_0 dx \\ \int_K f \psi_1 dx \\ \int_K f \psi_2 dx \end{bmatrix}. \end{aligned}$$

Thus, a large amount of meaningful information has been stored in multiscale basis functions through the mapping matrix  $R$ , in which every coarse element in each row and column contains local microscopic details. A reduced matrix  $A^c = RA^fR^T$  and a reduced vector  $b^c = Rb^f$  are delivered on the coarse level. As a result, the multiscale finite element method produces a reduced algebraic system for solving

$$A^c u_h = b^c, \quad (3.15)$$

so the multiscale solution  $u_h$  is available.

Note that Eq. (3.15) is very different from the finite element method, where Eq. (3.2) needs to be solved on the fine-scale level

$$A^f u_g = b^f, \quad (3.16)$$

so the Galerkin solution  $u_g$  is available.

For any non-trivial system, one may expect that when the finite element method is applied on a very fine mesh, the global system (3.16) can be quite massive. If we take a large integer  $M$  as the sub-partition number, the FEM can be solved on the fine-scale level  $\mathcal{O}(NM)$ . While this would yield a more accurate result than a multiscale global system (3.15) solved on a coarse-scale level  $\mathcal{O}(N)$ , it is because FEM on a globally fine scale consumes significantly more computational

resources, that it is able to win this unfair competition. However, sometimes the multiscale strategy on the coarse-scale level can outperform FEM on a fine-scale level. Furthermore, the multiscale strategy is superior to the FEM on a fine scale in terms of efficiency. Consequently, the novel multiscale finite element method is gaining preference over the traditional mode. The advantages are especially more significant in high-dimensional situations.

## 4. Multiscale error estimate

Graded mesh nodes  $x_i$  are generated from the iterative formula (2.4) for resolving the twin boundary layers. Let  $\bar{K}_i = [x_{i-1}, x_i]$  be the  $i$ -th coarse element which may be divided into  $M$  sub-elements as shown:

$$x_{i-1,j} = x_{i-1} + j \frac{h_i}{M}, \quad i = 1, 2, \dots, N, \quad j = 0, 1, \dots, M.$$

Since the multiscale basis functions  $\phi_i = \sum_{j=0}^M r_{ij} \psi_j$  work in the microscopic scale, and the multiscale solution  $u_h = \sum_{i=0}^{N_{b2}} u_i \phi_i$  works in the macroscopic scale, as a result the enriching data are delivered at both scales. Here  $N_{b2}$  is the coarse-scale graded mesh partition number in the multiscale FE scheme, unlike the  $N_{b1}$  is the fine-scale partition number in the FE scheme.

$L^2$  norm and  $H^1$  norm of errors are

$$\|u - u_h\|_0^2 = \int_{\Omega} (u - u_h)^2 dx,$$

$$\|u - u_h\|_1^2 = \int_{\Omega} [(u - u_h)^2 + (u' - u_h')^2] dx.$$

An energy norm related to the parameter  $\varepsilon$  is defined as

$$\|u - u_h\|_{\varepsilon}^2 = \|u - u_h\|_0^2 + \varepsilon \|u - u_h\|_1^2.$$

Functions with a subscript  $I$  denote the interpolations. Next an error estimate in the energy norm for the multiscale approximation on the graded mesh is to be presented.

**Assumption 4.1.** Assume that a small  $\varepsilon$  satisfies

$$\varepsilon \leq CN^{-1}. \quad (4.1)$$

**Assumption 4.2.** Assume that the derivative of the mesh-generating function  $g$  in (2.7) satisfies

$$\max |g'| \leq CN. \quad (4.2)$$

**Assumption 4.3.** Assume that the eigenvalue (1.3) satisfies

$$\mu_1^{-1} \leq CN^{-\theta}, \quad 0 < \theta \leq 1. \quad (4.3)$$

**Lemma 4.1.** As for the graded mesh (2.4), its mesh size  $h_i$  has

$$h_i \leq CN^{-1}. \quad (4.4)$$

**Proof.** The graded nodes are given by Eq. (2.6). Hence, we have

$$h_i = x_i - x_{i-1} = \alpha\varepsilon[g(t_i) - g(t_{i-1})] = \alpha\varepsilon[(t_i - t_{i-1})g'(t_{i-1})] \leq \alpha\varepsilon \frac{1}{N} \max |g'|,$$

Assumption 4.1 and Assumption 4.2 are used in the last step, then (4.4) holds.  $\square$

**Lemma 4.2.** *For simplicity, for the case of a left transition point, the mesh-characterizing function satisfies*

$$|\exp^{-p\mu_1 x \frac{N}{4}}| \leq N^{-\alpha}. \tag{4.5}$$

**Proof.** With the above definitions and notations, we have

$$\begin{aligned} \exp^{-p\mu_1 x \frac{N}{4}} &= \exp^{-p\mu_1 \tau} = \exp^{-p\mu_1 \alpha \varepsilon \log N} = \exp^{-\alpha \log N} \\ &= \exp^{-\alpha g(\frac{1}{4})} \leq \max\{N^{-\sigma}, \mu_1^{-\sigma}\} \leq N^{-\theta\sigma} \leq N^{-\alpha}, \end{aligned}$$

from Assumption 4.3 and set  $\sigma \geq \frac{\alpha}{\theta}$ ,  $0 < \theta \leq 1$ , then (4.5) holds.  $\square$

As above-mentioned, the domain is divided into a left singular component  $\Omega_1 = [0, \tau]$ , a right singular component  $\Omega_3 = [1 - \tau, 1]$  and an inner smooth component  $\Omega_2 = [\tau, 1 - \tau]$ . They are formed two dense and a sparse intervals on the graded mesh, respectively. For this quasi-symmetric discretization, let us focus on the left singular component  $\Omega_1$ . For the right singular component  $\Omega_3$ , the results are similar.

**Lemma 4.3.** *For the decomposition (1.5), in the whole domain and in its different intervals we have the following:*

$$\|S - S_I\|_{l, \Omega} \leq CN^{l-\alpha}, \quad 0 \leq l \leq k, \quad \alpha = k + 1, \tag{4.6}$$

$$\|E - E_I\|_{0, \Omega_1} \leq C\varepsilon^{\frac{1}{2}} N^{-1} \max |\omega'|^{k+\frac{1}{2}}, \tag{4.7}$$

$$\|E\|_{0, \Omega_2} \leq CN^{-\alpha}, \tag{4.8}$$

$$\|E_I\|_{0, \Omega_2} \leq CN^{-\alpha}. \tag{4.9}$$

**Proof.** As for (4.7), since

$$\begin{aligned} \|E - E_I\|_{0, \Omega_1} &\leq C\left(\frac{\tau}{N}\right)^\alpha, \\ |E - E_I|_{l, \Omega_1} &\leq Ch_i^{\alpha-l} |E|_{\alpha, \Omega_1}, \\ |E|_{\alpha, \Omega_1} &\leq C\varepsilon^{\frac{1}{2}} \left(\frac{\max |\omega'|}{N}\right)^\alpha, \end{aligned}$$

and from Lemma 4.1, it reads

$$\|E - E_I\|_{0, \Omega_1}^2 \leq C\varepsilon \frac{\max |\omega'|^{2k+1}}{N^2},$$

then (4.7) holds. As for (4.8), since

$$\begin{aligned} \|E\|_{0, \Omega_2} &\leq C \int_{\tau}^{1-\tau} \exp^{-\frac{\beta(1-x)}{\varepsilon}} dx \\ &\leq C\varepsilon \exp^{-\frac{\beta\tau}{\varepsilon}} \leq C\varepsilon \exp^{-\beta\alpha \log N} \leq CN^{-\alpha}, \end{aligned}$$

then (4.8) holds. Other proofs are omitted.  $\square$

**Lemma 4.4.** *Let  $u$ ,  $u_I$  be the exact solution and its interpolation of (1.8) respectively, then*

$$\|u - u_I\|_{0,\Omega} \leq C(N^{-\alpha} + \varepsilon^{\frac{1}{2}}N^{-1} \max |\omega'|^{k+\frac{1}{2}}). \quad (4.10)$$

**Proof.** From the decomposition (1.5),

$$\begin{aligned} \|u - u_I\|_{0,\Omega_1} &\leq \|S - S_I\|_{0,\Omega_1} + \|E - E_I\|_{0,\Omega_1} \\ &\leq C(N^{-\alpha} + \varepsilon^{\frac{1}{2}}N^{-1} \max |\omega'|^{k+\frac{1}{2}}), \\ \|u - u_I\|_{0,\Omega_2} &\leq \|S - S_I\|_{0,\Omega_2} + \|E\|_{0,\Omega_2} + \|E_I\|_{0,\Omega_2} \\ &\leq CN^{-\alpha} + CN^{-\alpha} + CN^{-\alpha} \\ &\leq CN^{-\alpha}, \end{aligned}$$

from Lemma 4.3 it holds.  $\square$

**Lemma 4.5.** [24] *Let  $u$ ,  $u_I$  be the exact solution and its interpolation of (1.8) respectively, then*

$$\varepsilon^{\frac{1}{2}}\|u - u_I\|_{1,\Omega} \leq C(h + N^{-1} \max |\omega'|). \quad (4.11)$$

The above lemmas are available, now we are ready to present the main theoretical result.

**Theorem 4.1.** *Let  $u$ ,  $u_h$  be the exact solution in (1.8) and the multiscale solution in (3.5) respectively, then for the energy norm it has*

$$\|u - u_h\|_{\varepsilon} \leq C_1N^{-\alpha} + C_2\varepsilon^{\frac{1}{2}}N^{-1} \max |\omega'|^{k+\frac{1}{2}}. \quad (4.12)$$

**Proof.** From the triangle inequality,

$$\|u - u_h\|_{\varepsilon} \leq \|u - u_I\|_{\varepsilon} + \|u_I - u_h\|_{\varepsilon}. \quad (4.13)$$

For the first term at the right side of (4.13), from Lemma 4.4, Lemma 4.5 and Assumption 4.1, we have

$$\|u - u_I\|_{\varepsilon} \leq C(N^{-\alpha} + \varepsilon^{\frac{1}{2}}N^{-1} \max |\omega'|^{k+\frac{1}{2}}). \quad (4.14)$$

For the second term at the right side of (4.13), denote the error by  $e = u_I - u_h$ . Since  $a(u - u_h, e) = 0$  and the bilinear form (1.6), it reads

$$\begin{aligned} \lambda\|u_I - u_h\|_{\varepsilon}^2 &= \lambda\|e\|_{\varepsilon}^2 \leq a(e, e) \\ &= a(u_I - u_h, e) = a(u_I - u + u - u_h, e) = a(u_I - u, e) \\ &= \varepsilon((u_I - u)', e') + (b(S_I - S)', e) - (b'(E_I - E), e) \\ &\quad - (b(E_I - E), e') + (c(u_I - u), e). \end{aligned}$$

In the last step, mainly consider the fourth item, since

$$\begin{aligned} |(b(E_I - E), e')|_{\Omega_1} &\leq C\|E_I - E\|_{\infty,\Omega_1}\|e'\|_{L^1(\Omega_1)} \\ &\leq CN^{-1} \max |\omega'|^{k+\frac{1}{2}}\|e\|_{\varepsilon}, \\ |(b(E_I - E), e')|_{\Omega_2} &\leq C\|E_I - E\|_{\infty,\Omega_2}N\|e\|_0 \\ &\leq CN^{-k}\|e\|_{\varepsilon}, \end{aligned}$$

so

$$|(b(E_I - E), e')|_{\Omega} \leq CN^{-1} \max |\omega'|^{k+\frac{1}{2}} \|e\|_{\varepsilon}.$$

Divided both sides of the inequality with  $\|e\|_{\varepsilon}$ , the estimate for  $\|u_I - u_h\|_{\varepsilon}$  is obtained. Combining this with Eq. (4.13), (4.14), Lemma 3.1, and Lemma 4.2, the proof is complete.  $\square$

**Remark 4.1.** In Theorem 4.1 and  $\alpha = k + 1$  for  $k = 1$  as linear basis functions are applied in the multiscale strategy, so that the second-order convergence is guaranteed from  $N^{-\alpha}$ . In addition, with the ingredients of the adaptively mesh-characterizing function  $\omega$  in the form of  $|\omega'|^{k+\frac{1}{2}}$ , as a consequence the multiscale finite element method would have the ability to achieve its potential superconvergence.

## 5. Numerical results

In this section, the singularly perturbed convection-diffusion model exhibiting twin boundary layers is solved numerically to test the behaviors of the proposed method. The multiscale finite element method is applied on the graded mesh (abbreviated as the MsFEM(G)), which is compared with the exact solution and other literature methods.

Error norms and convergence orders are measured as

$$\begin{aligned} Err_{\infty}(N) &= \|u - u_N\|_{L^{\infty}}, \\ Err_{en}(N) &= \|u - u_N\|_{\varepsilon}, \\ \text{order} &= \frac{\log Err(N) - \log Err(2N)}{\log 2}, \end{aligned}$$

where  $u_N$  is the numerical solution for the partition number  $N$ . Note that for the case of a graded mesh  $Err(N)$  is not from an exactly pre-determined  $N$ , but it is from its approximate equivalent  $N$  in (2.4). The same rule is applicable to its double refinement of  $Err(2N)$ .

**Example 5.1.** As a benchmark in the literature [13, 19–21, 23, 27] and  $b(x) = 4x - 2$ ,  $c(x) = 4$  is given in (1.1), an exact solution is

$$u(x) = \exp \frac{2x(x-1)}{\varepsilon}. \quad (5.1)$$

Now the right side is homogeneous  $f(x) = 0$ . Note that with a small parameter  $\varepsilon$  in this example, rapid jumps of  $u(x)$  are shown near the twin boundary sides  $x = 0$  and  $x = 1$ .

Figure 2 illustrates that the classical FEM on a uniform mesh fails to solve singularly perturbed problems with small parameters. This drawback may be overcome by using a non-uniform and a fitting mesh, or in other words, a graded mesh. Based on the multiscale finite element scheme for a relatively coarse number  $N = 30$ , the MsFEM(G) behaves well enough to be able to precisely approach the model's interior as well as the twin boundaries. The mesh is automatically concentrated at the location of the twin boundary layers, while it is quite sparse in the smooth, interior region of the model. In this way, the total partition number  $N$  is kept to save the computational storage and execution time. It is apparent in Figure 3 that

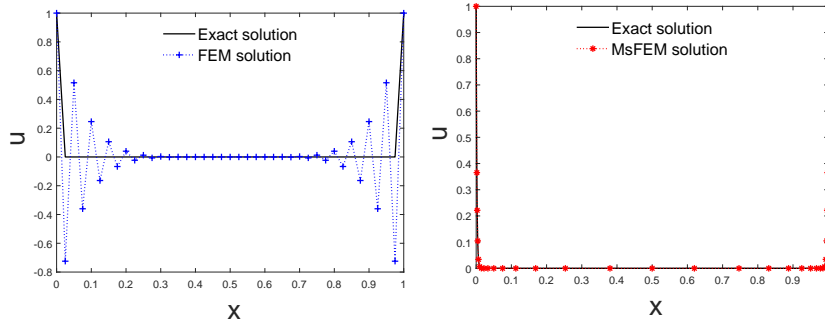


**Figure 2.** Exact and FEM solution on uniform mesh  $N = 40$  (left), exact and MsFEM solution on graded mesh  $N = 30$  (right), for Example 5.1 with  $\varepsilon = 2^{-8}$ .

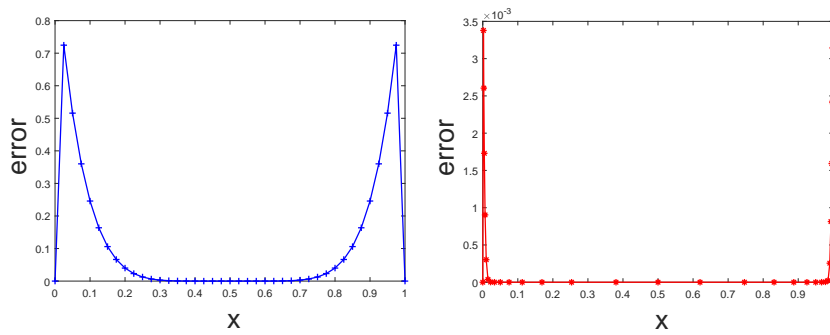


**Figure 3.** Errors of FEM(U) on  $N = 40$  and MsFEM(G) on  $N = 30$ , for Example 5.1 with  $\varepsilon = 2^{-8}$ .

**Table 1.** Comparison of  $Err_\infty$  for Example 5.1.

$\varepsilon$	$N = 128$				$\bar{N} = 120$	$N = 256$				$\bar{N} = 254$
	In [21]	In [19]	In [13]	In [23]	PM	In [21]	In [19]	In [13]	In [23]	PM
$2^{-8}$	6.8E-3	3.7E-3	3.3E-4	8.0E-5	1.4E-3	1.7E-3	7.8E-4	7.4E-5	2.0E-5	1.4E-3
$2^{-10}$	1.0E-2	8.3E-3	4.7E-3	7.2E-5	3.9E-4	2.6E-3	3.2E-3	1.2E-4	1.7E-5	3.6E-4
$2^{-12}$	1.5E-2	8.0E-3	8.2E-2	7.0E-5	1.2E-4	3.7E-3	4.0E-3	1.7E-3	1.7E-5	9.5E-5

**Table 2.** Comparison of  $Err_\infty$  for Example 5.1.

$\varepsilon$	$N = 128$			$\bar{N} = 182$	$N = 256$			$\bar{N} = 376$
	In [27]	In [20]	In [23]	PM	In [27]	In [20]	In [23]	PM
$10^{-2}$	4.87E-2	2.19E-3	9.87E-5	3.72E-3	2.93E-2	7.21E-4	2.65E-5	3.70E-3
$10^{-4}$	4.95E-2	2.34E-3	6.96E-5	8.28E-5	2.98E-2	8.22E-4	1.65E-5	4.28E-5
$10^{-6}$	4.95E-2	2.34E-3	6.93E-5	6.36E-5	2.98E-2	8.21E-4	1.64E-5	9.30E-6
$10^{-8}$	4.95E-2	2.34E-3	6.93E-5	6.34E-5	2.98E-2	8.21E-4	1.64E-5	9.12E-6

the corresponding errors are greatly improved, whose maximum error is reduced from 0.8 to  $3.5 \times 10^{-3}$  in the multiscale FEM on the coarse graded mesh.

Several literature results are listed and compared with our proposed method, in Table 1 and Table 2 with different values of  $\varepsilon$ . Note that since the partition number  $N$  in a graded mesh is automatically generated from Eq. (2.4), it depends on the

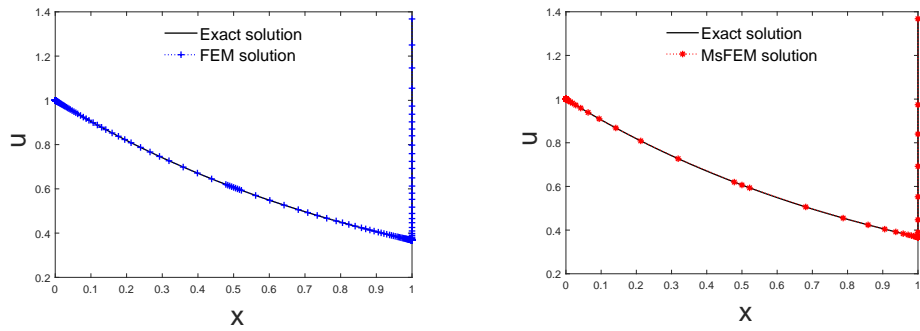


**Figure 4.** Exact and FEM solution on fine graded mesh  $N = 424$  (left), exact and MsFEM solution on coarse graded mesh  $N = 106$  (right), for Example 5.2 with  $\varepsilon = 10^{-9}$ .

corresponding value of  $\varepsilon$ . In the tables an average partition number  $\bar{N}$ , which is chosen to be almost equal as in other literature to be fairly compared. It is seen in Table 1 that the  $Err_{\infty}$  accuracy of the proposed method is significantly better than the previous three works, even though it is not superior to the fourth work. However, it is crucial to point out that a quintic B-spline collocation method is employed in [23]. While in our method, just the multiscale linear basis functions in the Lagrange style are used in the local problem (3.4) for this accuracy. As a result, its computational costs are much reduced. Another encouraging fact is in Table 2 that for very small parameters such as  $\varepsilon = 10^{-6}$  and  $10^{-8}$ , the MsFEM(G) equipped with the linear multiscale bases outperforms to the quintic B-spline collocation in [23].

**Example 5.2.** Set  $b(x) = 1$ ,  $c(x) = 1 + \varepsilon$  and an exact solution is available as

$$u(x) = \exp^{-x} + \exp^{\frac{x-1}{\varepsilon}}. \quad (5.2)$$

Then a non-homogeneous right side  $f(x) = (1 + \varepsilon) \exp^{\frac{x-1}{\varepsilon}}$ . It is known that boundary layers phenomena are dominated at the twin boundary sides as for the small  $\varepsilon$ . We know that the FEM on the uniform mesh can not reliably solve this dilemma, and there is no literature available for comparison. We apply the multiscale FEM with a graded mesh refinement directly.

In Table 3, it can be seen that a larger partition number  $N$  is necessary for very small values of the parameter  $\varepsilon$ , to resolve the twin boundary oscillations. With the graded mesh recursion (2.4), we find that an almost linear increase in  $N$  is sufficient to capture the singular perturbation. To test the history of convergence order of  $Err_{\infty}$  and  $Err_{en}$  norms, the graded mesh was almost redoubled, and the multiscale finite element method on the coarse mesh was observed to achieve second-order convergence in the  $Err_{\infty}$  norm, and superconvergence with a second-order in the  $Err_{en}$  norm, which is in accordance to (4.12) in Theorem 4.1. The fact that the results were independent of the values of perturbation parameter  $\varepsilon$  was validated to show the parameter-uniform property. Please note that the multiscale scheme just operates through the linear basis functions and runs on the graded mesh of coarse-scale level. Therefore, while ensuring accuracy, the proposed method also needs significantly less computational resources. We encourage its use with large partition numbers and problems featuring large dimensions.

A visual comparison of the exact and numerical solutions and their correspond-

**Table 3.**  $Err_\infty$ ,  $Err_{en}$  and convergence order of MsFEM(G) for Example 5.2.

$\varepsilon = 10^{-1}$				
$N$	$Err_\infty$	order	$Err_{en}$	order
14	7.846E-4		4.736E-3	
30	2.063E-4	1.93	9.856E-4	2.26
66	5.543E-5	1.90	1.962E-4	2.33
148	1.444E-5	1.94	3.921E-5	2.32
332	3.690E-6	1.97	8.079E-6	2.28
748	9.337E-7	1.98	1.702E-6	2.25
1664	2.351E-7	1.99	3.683E-7	2.21
3674	5.895E-8	2.00	8.137E-8	2.18
$\varepsilon = 10^{-8}$				
$N$	$Err_\infty$	order	$Err_{en}$	order
94	4.037E-4		4.822E-4	
174	1.191E-4	1.76	1.189E-4	2.03
340	3.277E-5	1.86	2.768E-5	2.10
680	8.630E-6	1.92	6.453E-6	2.10
1380	2.217E-6	1.97	1.520E-6	2.09
2826	5.619E-7	1.98	3.609E-7	2.08
5806	1.414E-7	1.99	8.622E-8	2.07
11942	3.543E-8	2.00	2.073E-8	2.06
$\varepsilon = 10^{-10}$				
$N$	$Err_\infty$	order	$Err_{en}$	order
116	4.037E-4		3.871E-4	
216	1.191E-4	1.76	9.457E-5	2.03
418	3.277E-5	1.86	2.219E-5	2.10
832	8.630E-6	1.92	5.195E-6	2.09
1680	2.217E-6	1.97	1.234E-6	2.08
3420	5.619E-7	1.98	2.978E-7	2.05
6990	1.414E-7	1.99	7.312E-8	2.03
14304	3.543E-8	2.00	1.705E-8	2.10

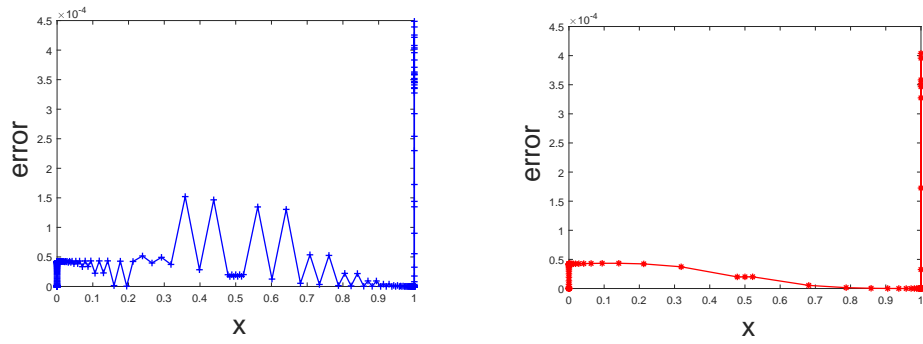


**Figure 5.** Errors of FEM(G) on fine mesh  $N = 424$  and MsFEM(G) on coarse mesh  $N = 106$ , for Example 5.2 with  $\varepsilon = 10^{-9}$ .

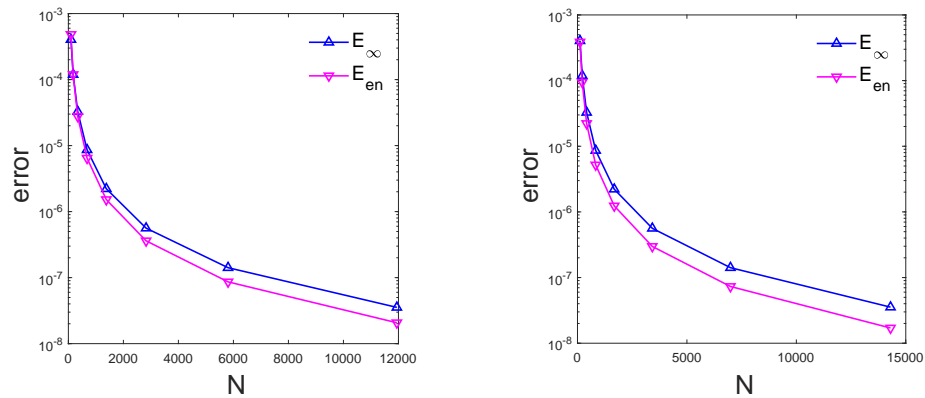


**Figure 6.** Convergence history for  $Err_\infty$ ,  $Err_{en}$  of MsFEM(G), for Example 2 with  $\varepsilon = 10^{-8}$  (left) and  $10^{-10}$  (right), respectively.

ing errors is shown in Figures 4 and 5. Figure 4 shows that the graded mesh enabled both FEM and MsFEM to effectively capture the exact twin boundaries. However, the multiscale strategy needs  $N = 106$  to achieve the same level of accuracy that FEM needed  $N = 424$  to achieve, which is four times that needed by the multiscale strategy. Thus, it is evident that given the same computational resources, the multiscale strategy could potentially be used for applications involving much larger dimensions than what FEM would be able to do. The maximum errors are both  $4.5 \times 10^{-4}$  and they dominate mainly on the right side in Figure 5, while the discrete error of MsFEM(G) is relatively smooth in the domain.

We have thus demonstrated that for small parameters  $\varepsilon = 10^{-8}, 10^{-10}$  (Figure 6) that the convergence order of the energy norm  $Err_{en}$  is higher than the second-order of  $Err_\infty$ . The theoretical results from Eq. (4.12) were thus verified numerically.

## 6. Conclusion

A robust and efficient strategy of the multiscale finite element method is presented to address the singular perturbation problems. A graded mesh was constructed in an adaptive manner for capturing local microscopic oscillations. With the help

of multiscale linear basis functions on the local level, detailed mapping behaviors among the scales were delivered and then enriched into its multiscale scheme. As a result, the multiscale solution was able to approach the exact solution almost perfectly on the global level. The superconvergence theorem for error estimation in the energy norm was proved. The ability of the multiscale scheme was validated numerically. It was shown to be accurate and effective irrespective of the perturbation parameter values. For the convection-diffusion model, our proposed method provides a parameter-uniform superconvergence in the energy norm, without being very computationally intense. The advantages of the multiscale finite element method on graded meshes are quite promising for applications involving large dimensions.

## Acknowledgements

We would like to thank the referees and editors for their insightful comments and helpful suggestions, which led to an improvement of the paper.

## References

- [1] M. Brdar, G. Radojev, H. G. Roos and L. Teofanov, *Superconvergence analysis of FEM and SDFEM on graded meshes for a problem with characteristic layers*, *Comput. Math. Appl.*, 2021, 93, 50–57.
- [2] M. Brdar and H. Zarin, *A singularly perturbed problem with two parameters on a Bakhvalov-type mesh*, *J. Comput. Appl. Math.*, 2016, 292, 307–319.
- [3] M. Brdar, H. Zarin and L. Teofanov, *A singularly perturbed problem with two parameters in two dimensions on graded meshes*, *Comput. Math. Appl.*, 2016, 72, 2582–2603.
- [4] D. F. Cai, Z. Q. Cai and S. Zhang, *Robust equilibrated a posteriori error estimator for higher order finite element approximations to diffusion problems*, *Numer. Math.*, 2020, 144, 1–21.
- [5] Z. D. Cen, A. M. Xu and A. B. Le, *A high-order finite difference scheme for a singularly perturbed fourth-order ordinary differential equation*, *Inter. J. Comput. Math.*, 2018, 95(9), 1–14.
- [6] Y. Cheng, *On the local discontinuous Galerkin method for singularly perturbed problem with two parameters*, *J. Comput. Appl. Math.*, 2021, 392, 113485.
- [7] Y. Cheng, S. Jiang and M. Stynes, *Supercloseness of the local discontinuous Galerkin method for a singularly perturbed convection-diffusion problem*, *Math. Comput.*, 2023, 92(343), 2065–2095.
- [8] Y. Cheng, Y. J. Mei and H. G. Roos, *The local discontinuous Galerkin method on layer-adapted meshes for time-dependent singularly perturbed convection-diffusion problems*, *Comput. Math. Appl.*, 2022, 117, 245–256.
- [9] E. Chung and Y. B. Li, *Adaptive generalized multiscale finite element methods for  $H(\text{curl})$ -elliptic problems with heterogeneous coefficients*, *J. Computat. Appl. Math.*, 2019, 345, 357–373.
- [10] P. Constantinou, S. Franz, L. Ludwig and C. Xenophontos, *Finite element approximation of reaction-diffusion problems using an exponentially graded mesh*, *Comput. Math. Appl.*, 2018, 76, 2523–2534.

- [11] R. G. Durán and A. L. Lombardi, *Finite element approximation of convection diffusion problems using graded meshes*, Appl. Numer. Math., 2006, 56, 1314–1325.
- [12] E. G. M. Elmahdi and J. F. Huang, *Efficient numerical solution of two-dimensional time-space fractional nonlinear diffusion-wave equations with initial singularity*, J. Appl. Anal. Comput., 2022, 12(2), 831–849.
- [13] F. Z. Geng and S. P. Qian, *Reproducing kernel method for singularly perturbed turning point problems having twin boundary layers*, Appl. Math. Letters, 2013, 26, 998–1004.
- [14] L. Govindarao and J. Mohapatra, *A numerical scheme to solve mixed parabolic-elliptic problem involving singular perturbation*, Inter. J. Comput. Math, 2022, 99(10), 2069–2090.
- [15] V. Gupta, M. K. Kadalbajoo and R. K. Dubey, *A parameter-uniform higher order finite difference scheme for singularly perturbed time-dependent parabolic problem with two small parameters*, Inter. J. Comput. Math., 2019, 96(3), 474–499.
- [16] S. Jiang, L. Liang, M. L. Sun and F. Su, *Uniform high-order convergence of multiscale finite element computation on a graded recursion for singular perturbation*, Electr. Research Archive, 2020, 28(2), 935–949.
- [17] S. Jiang, M. Presho and Y. Q. Huang, *An adapted Petrov-Galerkin multiscale finite element for singularly perturbed reaction-diffusion problems*, Inter. J. Comput. Math., 2016, 93(7), 1200–1211.
- [18] S. Jiang, M. L. Sun and Y. Yang, *Reduced multiscale computation on adapted grid for the convection-diffusion Robin problem*, J. Appl. Anal. Comput., 2017, 7(4), 1488–1502.
- [19] M. K. Kadalbajoo, P. Arora and V. Gupta, *Collocation method using artificial viscosity for solving stiff singularly perturbed turning point problem having twin boundary layers*, Comput. Math. Appl., 2011, 61, 1595–1607.
- [20] M. K. Kadalbajoo and V. Gupta, *A parameter uniform B-spline collocation method for solving singularly perturbed turning point problem having twin boundary layers*, Inter. J. Comput. Math., 2010, 87(14), 3218–3235.
- [21] M. K. Kadalbajoo and K. C. Patidar, *Variable mesh spline approximation method for solving singularly perturbed turning point problems having boundary layer(s)*, Comput. Math. Appl., 2001, 42, 1439–1453.
- [22] A. Kaushik, A. K. Vashishth, V. Kumar and M. Sharma, *A modified graded mesh and higher order finite element approximation for singular perturbation problems*, J. Comput. Physics, 2019, 395, 275–285.
- [23] D. Kumar, *A parameter-uniform method for singularly perturbed turning point problems exhibiting interior or twin boundary layers*, Inter. J. Comput. Math., 2019, 96(5), 865–882.
- [24] T. Linb, *Layer-adapted meshes for convection-diffusion problems*, Comput. Method. Appl. Mech. Engin., 2003, 192, 1061–1105.
- [25] X. W. Liu and J. Zhang, *Galerkin finite element methods for convection-diffusion problems with exponential layers on Shishkin triangular meshes and hybrid meshes*, Appl. Math. Comput., 2017, 307, 244–256.

- 
- [26] R. K. Lodhi and H. K. Mishra, *Quintic B-spline method for solving second order linear and nonlinear singularly perturbed two-point boundary value problems*, J. Comput. Appl. Math., 2017, 319, 170–187.
- [27] S. Natesan, J. Jayakumar and J. Vigo-Aguiar, *Parameter-uniform numerical method for singularly perturbed turning point problems exhibiting boundary layers*, J. Comput. Appl. Math., 2003, 158, 121–134.
- [28] E. Oriordan, M. L. Pickett and G. I. Shishkin, *Parameter-uniform finite difference schemes for singularly perturbed parabolic diffusion-convection-reaction problems*, Math. Comput., 2006, 75, 1135–1154.
- [29] H. G. Roos, L. Teofanov and Z. Uzelac, *A modified Bakhvalov mesh*, Appl. Math. Letters, 2014, 31, 7–11.
- [30] H. G. Roos, L. Teofanov and Z. Uzelac, *Graded meshes for higher order FEM*, J. Comput. Math., 2015, 33, 1–16.
- [31] K. K. Sharma, P. Rai and K. C. Patidar, *A review on singularly perturbed differential equations with turning points and interior layers*, Appl. Math. Comput., 2013, 219, 10575–10609.
- [32] Q. Yang and M. K. Ni, *Asymptotics of a class of singularly perturbed weak nonlinear boundary value problem with a multiple root of the degenerate equation*, J. Nonlinear Model. Anal., 2022, 4(3), 502–513.
- [33] Y. H. Yin and P. Zhu, *The streamline-diffusion finite element method on graded meshes for a convection-diffusion problem*, Appl. Numer. Math., 2019, 138, 19–29.